Analysis and Implications of Transition-Band Signals in High-Resolution NMR

Csaba Szántay, Jr.

Spectroscopic Research Division, Gedeon Richter Ltd., POB 27, H-1475 Budapest, 10, Hungary

The problem of signals generated in and received from regions outside the active coil area is discussed in the context of using standard measurement techniques. Some of the conceptual and practical consequences of the existence of such transition-band signals are highlighted. Examples include radiation damping, pulse-width calibration, lineshape and radiofrequency homogeneity tests, improper saturation, and exchange- and relaxation-rate determinations. One interesting implication is that apparent sample-to-sample variations in the calibrated 90° pulse width values are a function not only of probe tuning and bulk susceptibility effects, but also of the linewidths involved. A semi-quantitative treatment of the phenomenon is also given. © 1998 Academic Press

Key Words: **high-resolution NMR; transition-band signals; lineshape; Bloch simulation; implications.**

In high-resolution NMR the sample is routinely prepared such that it extends well over the active radiofrequency (rf) transmitter/receiver coil area in order to avoid lineshape distortions caused by susceptibility discontinuities at the ends of the sample volume and sample tube. As required in most applications, the coil produces a spatially almost uniform γB_1 field strength within its active area embracing a ca. 10-mm-long region of the sample along the z axis. Ideally, the $\gamma B_1(z)$ function should be rectangular, i.e., constant along the active (a) sample height Δz^a [$\gamma B_1^a(z)$ = constant] and falling instantly to zero at the upper and lower edges of the coil. While the first requirement can be adequately realized, in practice the sharp drop in γB_1 is unattainable. Consequently the total sample volume consists not only of nearly uniformly excited Δz^a and unexcited vertical layers, but also of intermediate, weakly excited "transition band" (tr) regions Δz^{tr} within which $\gamma B_1^{tr}(z)$ decreases from its maximum value to zero ([1]). According to Jahnke's measurements ([2]), the upper and lower transition bands add up to cover approximately a similar vertical region as the active sample volume itself.

Apart from a few examples ([1, 2]), the existence of signals generated in and received from the transition bands has been an almost completely ignored phenomenon in the high-resolution NMR literature, in line with the notion that, being not only weakly excited but also weakly detected ([2]), such "extraterrestrial" signals are so small as to be safely disregarded in most applications. Within the framework of this optimistic stance, two articles note that transition-band signals may be undesired and discuss their possible elimination by restricting the sample volume using a microcell ([2]) or its suppression via a complex scheme of gradient slice-selection techniques applied to a selectively excited resonance ([1]). Although both methods are useful in their own right, the first one involves some inconvenient sample preparation, sensitivity, and B_0 field inhomogeneity problems, while the second one, in addition to possibly being difficult to implement, does not solve the problem that a hard read pulse excites transition-band spins throughout the spectrum. Therefore, none of these techniques have become standard NMR tools.

So far a study of the main characteristics of transition-band signals has not been reported. In this article I will attempt to bring the issue into focus in the context of using standard measurement techniques. Some of the conceptual and practical implications of transition-band signals will also be highlighted. Examples involve radiation damping, pulse-width calibration, lineshape and rf homogeneity tests, residual signals upon saturation, and exchange- and relaxation-rate determinations. A semi-quantitative treatment of the phenomenon will also be given.

The material used as the primary experimental subject for exploring the main features of ^1H transition-band signals was simply a concentrated solution of chloroform dissolved in DMSO-d_6. For further demonstration some more complex systems were also studied.

All NMR measurements reported here were carried out with a latest-generation Varian 5-mm $^1H\{^{15}N-^{31}P\}$ PFG Indirect · nmr probe (300 MHz) on a Varian INOVA 300 instrument ([3a]). The presence of transition-band responses was also checked and verified on the following probes and instruments: (a) Varian 5-mm $^1H/^{19}F/^{15}N-^{31}P/$(old) switchable probe (300 MHz), Varian INOVA 300 spectrometer ([3a]); (b) Varian 5-mm $^1H\{^{15}N-^{31}P\}$ PFG Indirect · nmr probe (400 MHz), Varian INOVA 400 spectrometer ([3b]); (c) Varian ^1H 4-mm (40 μl) Nano · nmr probe (400 MHz), Varian INOVA 400 spectrometer ([3b]); (d) Varian 5-mm $^1H\{^{15}N-^{31}P\}$ PFG Indirect · nmr probe (500 MHz), Varian INOVA 500 spectrometer ([3a]); (e) Varian 5-mm $^1H\{^{13}C/^{15}N\}$ PFG Triple · nmr probe (500

MHz), Varian INOVA 500 spectrometer (*3a*); Bruker 5-mm ^{1}H{^{31}P–$^{107/109}$Ag} PFG probe, Bruker Avance DRX-500 spectrometer (*3c*); Bruker 5-mm triple-resonance ^{1}H{^{13}C/^{15}N} PFG probe, Bruker Avance DRX-500 spectrometer (*3d*). In each case transition bands were present and were very similar in their defining characteristics, although some differences in finer details were observed owing to the specifics of probe architecture. The problem seems to be universal in terms of probe design as well as generation type.

OVERVIEW OF THE PROBLEM

The rf field experienced by the transition region Δz^{tr} is inhomogeneous due to its spatial gradient ΔB_1^{tr}. If a pulse of nominal strength γB_1^a and duration pw produces a flip angle θ^a within the active sample region, transition-band spins experience an effective field $\gamma B_1^{tr} < \gamma B_1^a$ and an effective flip angle $\theta^{tr} < \theta^a$. In most applications transition-band signals are overshadowed by the much larger active-volume transverse magnetization generated by typical read pulses. A common manifestation of transition-band signals is seen, however, when this main transverse component is eliminated by a 180° or 360° pulse. In practice a small signal is nevertheless detected which stems from the transition-band spins whose more sluggish pulse response gives rise to an observable transverse magnetization which is easily mistaken for a lineshape-distorted form of the main signal itself. An example is seen near the null points of pw-arrayed CHCl$_3$ ^{1}H spectra (Fig. 1a). Note that from the perspective offered by Fig. 1a the transition-band problem appears relatively "harmless," a point to be disproved below.

There appears to be some confusion in the NMR literature about the exact source of such null-point artifacts. The phenomenon is usually interpreted, not necessarily in the context of transition bands, in terms of the co-occurrence of B_1 and B_0 inhomogeneities (*2, 4a, 5*). When discussed in relation to transition bands, the artifact is rationalized (*2, 5*) according to the concept that in addition to B_1 inhomogeneity being manifested in the $\gamma B_1^{tr} < \gamma B_1^a$ relationship, the Δz^{tr} spins are also broadened and slightly shifted in resonance frequency with respect to Δz^a spins due to B_0 inhomogeneity; this may suggest that with good shimming such "rogue" signals can be eliminated, since the main-field inhomogeneity factor is removed from the problem. (As shown below, Δz^{tr} spins can actually interfere with NMR experiments by having a "life of their own" that is unrelated to B_0 homogeneity.) Elsewhere, null-point distortions are described (*6*), not in connection with transition bands, but solely as caused by a spatially very inhomogeneous B_1 field which results in some sample regions experiencing slightly greater or slightly smaller γB_1 values than the applied nominal γB_1 field strength. On any modern spectrometer, excellent B_1 homogeneity within the active sample volume is, of course, a standard feature, while conspicuous

null-point artifacts can nevertheless be observed (Fig. 1a); thus the above explanation is misleading. Null-point artifacts are also cited as being indicative of unshielded probe coil lead pickup; this suggests a probe manufacturing problem that should be corrected by a lead shield (*7*). The null-point anomalies demonstrated below clearly originate from the Δz^{tr} region rather than improper shielding. [In our case, as expected from $\gamma B_1(z)$ field plots of well-designed probes (*1, 2, 7–9*), the water-drop test (*7*) revealed no lead pickup.]

PRELIMINARY EXPERIMENTAL AND CONCEPTUAL CONSIDERATIONS

In the $x'y'z$ rotating frame a B_1 field taken to be stationary along the x' axis causes spins, assumed to be resonant with the irradiation, to nutate in the zy' plane with γB_1 angular frequency. The spatially inhomogeneous ΔB_1^{tr} field of the region Δz^{tr} is then associated with a range of nutational frequencies $\gamma \Delta B_1^{tr}$. By envisioning Δz^{tr} as consisting of very thin δz^{tr} isochromatic regions of homogeneous δB_1^{tr} field such that $\Delta z^{tr} = \Sigma \, \delta z^{tr}$, we may anticipate the phenomenon of phase randomization (*8*), i.e., the rapid dephasing, in a characteristic time $T_{2\rho}^*$, of isochromatic transition-band spins during transient nutation about x'. It is tempting to argue that with increasing pw the transition-band signal simply disappears due to a quick destruction of its net observable magnetization as spins fan out in the zy' plane.

However, a closer look at the experimental behavior of transition-band signals indicates that a more subtle picture should in fact be invoked. Figure 2 shows the experimental lineshape (nonspinning) of the CHCl$_3$ ^{1}H resonance where the transverse component of $\mathbf{M}^a$ was attenuated by using (a) an active-volume pulse angle $\theta^a = 180° + \delta$ (δ denotes a small positive angle) and (b) $\theta^a = 360° + \delta$. In case (a) the active-volume peak has turned negative, but transition-band spins, having experienced an effective pulse angle $\theta^{tr} < 180°$, are detected as (broad) positive wings. In Fig. 2b the active-volume peak has turned positive, and the wings appear to split into a pair of narrower negative inner wings and a pair of broader positive outer wings.

By giving advance credit to the experimental results and rationalization offered below, it now proves useful to postulate that the observed inner and outer wings originate from two distinct ensembles of isochromatic δz layers (whatever the exact position of those layers within Δz^{tr} might be), denoted as regions $\Delta z^b = \Sigma \, \delta z^b$ and $\Delta z^c = \Sigma \, \delta z^c$, respectively (note that this definition allows for $\Delta z^b + \Delta z^c < \Delta z^{tr}$). Thus the total *detected* sample volume is modeled as comprising three main regions: Δz^a, Δz^b, and Δz^c. Each region is then associated with a net magnetization $\mathbf{M}^i$, *average* experienced rf power γB_1^i, rf inhomogeneity $\gamma \Delta B_1^i$, and time constants $T_{2\rho}^{i*}$ and T_2^{i*} where $i =$ a, b or c (T_1 and T_2 are assumed to be invariant along z). Thus in Fig. 2a, where $\theta^a = 180° + \delta$, the broad positive
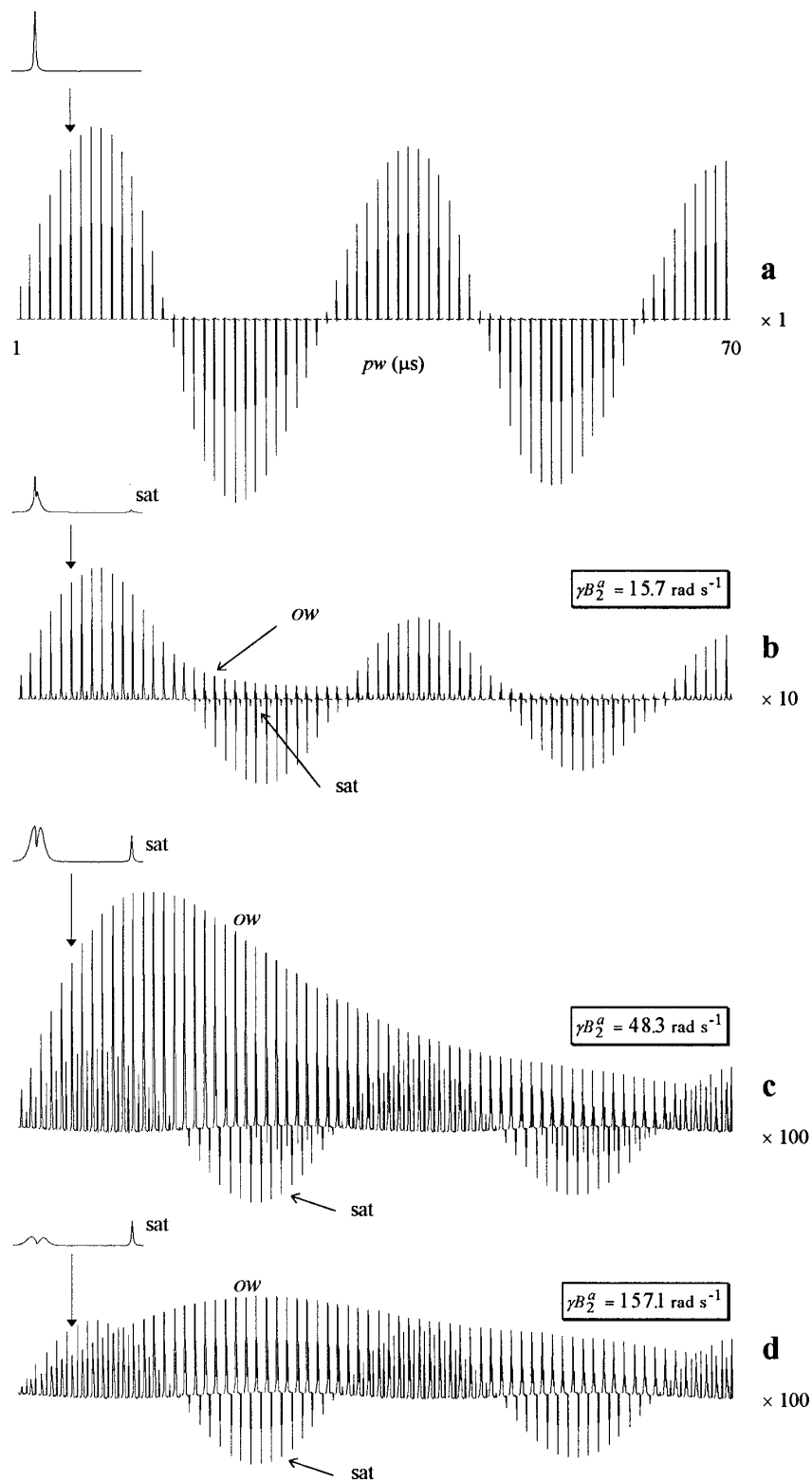
FIG. 1. Pulse width (pw) dependence of the $CHCl_3$ ^1H resonance (concentrated, nonspinning sample, 300 MHz, $T_1 \approx 10$ s from inversion-recovery experiments) obtained with $\gamma B_1^a = 2.067 \times 10^5$ rad s^{-1} on-resonance pulses (the 90° pulse width pw$_{90}$ is 7.6 μs for the active volume), pw incremented in 1-μs steps, four transients collected for each pw. (a) Normal conditions, relaxation delay 60 s. (b, c, d) A continuous on-resonance presaturating field B_2 was applied (decoupler channel) for 60 s prior to acquisition (no relaxation delay) at various precalibrated γB_2^a power levels, exposing the nonoscillatory behavior of the outer wing (ow) originating from the Δz^c region of the transition band. Vertical scales were increased with respect to (a) as denoted. For each array the plotted units show the active-volume $CHCl_3$ resonance and one oscillating ^{13}C satellite that is unaffected by B_2 and is 110 Hz upfield of the main peak.
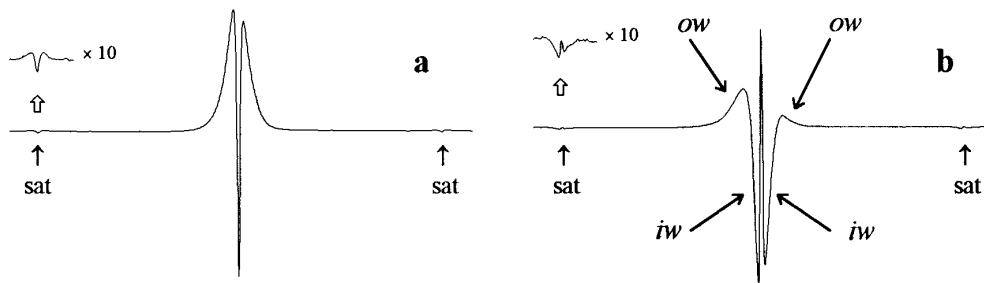
FIG. 2. CHCl$_3$ ^{1}H resonance (nonspinning) obtained with the transmitter set on-resonance and an active-volume flip angle θ^a that is (a) slightly greater than 180° and (b) slightly greater than 360°. (a) The narrow main peak due to $\mathbf{M}^a$ already turns negative, while the broader wings originating from $\Delta z^b + \Delta z^c$ are still positive ($\theta^{tr} < 180°$). (b) The main peak has turned positive, and the wings break into two distinct parts: a narrower inner wing (iw) associated with Δz^b ($180° < \theta^b < 360°$), and a broader positive outer wing (ow) associated with Δz^c. The ^{13}C satellite signals are accompanied by similar transition-band responses as the main resonance.

resonance comes from the transverse components $M^b_{x'y'} + M^c_{x'y'}$ in accord with $\theta^{b,c} < 180°$. In Fig. 2b, where $\theta^a = 360° + \delta$, the inner wings correspond to $180° < \theta^b < 360°$ and the outer wings to $\theta^c < 180°$ (as shown below, θ^c can actually never reach 90°), which is indicative of a $\gamma B_1^a > \gamma B_1^b > \gamma B_1^c$ relationship.

Further insight is gained by looking at the process "in motion" as $\mathbf{M}^a$, $\mathbf{M}^b$, and $\mathbf{M}^c$ nutate in the Bloch sphere (Fig. 3). As the main peak passes through $\theta^a = 180°$ (nadir-pass #1), the wings due to $\Delta z^b + \Delta z^c$ remain positive. As the active-volume signal goes through $\theta^a = 360°$ (zenith-pass #1), the inner wings due to Δz^b lag behind, while the outer wings due to Δz^c remain positive. The slower oscillation of the inner wings can be tracked by monitoring further revolutions of the net magnetizations (passes #2, #3 and #4). On subsequent nadir-passes the lineshape becomes less well defined as compared to pass #1, partly because off-resonance effects cumulate with the number of revolutions in the nadir area. This appears to be less of a problem for zenith passes, where off-resonance errors tend to be self-compensating.

Although the outer wings stay positive in round #1 (and its remnants are still visible in round #2), they fade away in further rounds and become difficult to detect beside the main signal and the inner wings. More direct experimental evidence regarding their behavior comes from using a long continuous presaturating field B_2 targeted at the main signal of the CHCl$_3$ resonance (Figs. 1b, 1c, and 1d). While the main signal and the inner wings are easily subdued, the outer wings are quite insensitive to saturation. Application of a relatively mild saturation power (Fig. 1b) leaves some residual active-volume signal whose oscillatory pulse width dependence is unaffected; in addition, the outer wings show aperiodic progress toward steady state. When an appropriately strong γB_2^a field is applied which completely suppresses the main signal as well as the inner wings, but causes only mild saturation within Δz^c (Figs. 1c and 1d), the residual outer wings give an even more conspicuous nonoscillatory pulse-width dependence.

To rationalize the above behavior, we must consider the following. Under the influence of on-resonance rf irradiation, the net moment vector $\mathbf{M}$ decays in a characteristic damping time $T^*_{2\rho}$ (or rate constant $R^*_{2\rho}$) defined (10, 11) as

$$\frac{1}{T^*_{2\rho}} = R^*_{2\rho} = \frac{1}{2}\left(\frac{1}{T_1} + \frac{1}{T^*_2}\right) + \gamma\Delta B_1, \qquad [1]$$

where the first term represents the shrinkage of $\mathbf{M}$ due to relaxation (T_1 and T^*_2 have their usual meaning) and B_1 has an inhomogeneity on the order ΔB_1. [Equation [1] rests on the implicit and simplistic assumption that the decay caused by rf inhomogeneity is exponential (10).] Two main scenarios should be distinguished: (a) for $\gamma B_1 > R^*_{2\rho}$ the motion of $\mathbf{M}$ is *underdamped,* i.e., a periodic nutation combined with slow damping due to relaxation and rf inhomogeneity; (b) in the limit of $\gamma B_1 < R^*_{2\rho}$, $\mathbf{M}$ shows an *overdamped,* nonoscillatory time evolution. [For active-volume spins experiencing good rf homogeneity and having natural relaxation times on the order of seconds, whether the spin response is underdamped or overdamped typically depends on whether the B_1 irradiation falls in the "high-power" or the frequency-selective "low-power" (12) category.] When only the relaxation term in Eq. [1] is taken into account, both cases can be accurately described by the complex analytical solutions of the generalized Bloch equations (13, 14). In typical cases where T_1 and T^*_2 are on the order of seconds, for a hard pulse with γB_1^a on the order of 10^5 rad s^{-1}, the mild damping of $\mathbf{M}^a$ observed on the microseconds timescale (Fig. 1a) is due to a slight rf inhomogeneity rather than relaxation. ΔB_1^b and ΔB_1^c are much larger than ΔB_1^a, and since the $\gamma B_1(z)$ function is not known in detail, the inhomogeneity term ΔB_1 precludes the accurate calculation of the magnetization trajectory, particularly in the limit of overdamping.

In line with Figs. 1–3, the above classification readily offers a model according to which spins in the Δz^a and Δz^b regions
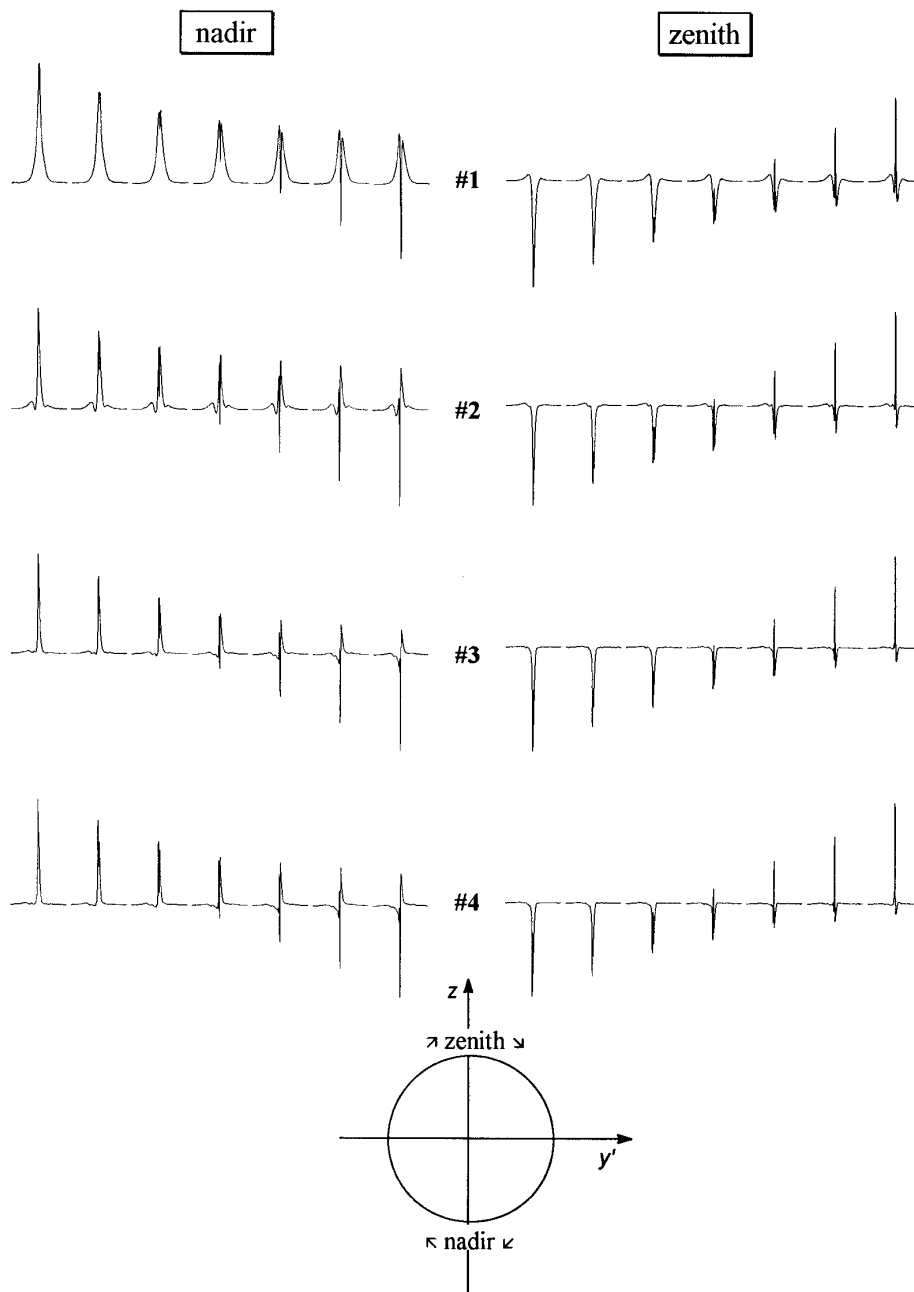
FIG. 3. Lineshapes obtained as the active-volume $CHCl_3$ ^1H resonance (nonspinning, transmitter on-resonance, B_1 assumed to be along the x' axis) nutates in the zy' plane of the Bloch sphere and passes through the $-z$ axis ("nadir-pass") and the $+z$ axis ("zenith-pass") in four subsequent revolutions. (Nadir-pass #1 corresponds to the vicinity of $\theta^a = 180°$ and zenith-pass #1 to that of $\theta^a = 360°$.) For each pass, pw ($\gamma B_1^a = 2.067 \times 10^5$ rad s^{-1}) was incremented in 0.1-μs steps.

give a slightly and significantly *underdamped,* while those in Δz^c give an *overdamped* response to the applied pulse.

In the Δz^a area a hard pulse of course delivers high-power irradiation for which $\gamma B_1^a \gg R_{2\rho}^{a*}$. With the initial condition $M_z^a = M_0^a$ and $M_{x'}^a = M_{y'}^a = 0$, after the resonant B_1 field has been turned on along x', $\mathbf{M}^a$ will nutate about x' to give a damped intensity fluctuation of the approximate form (*12*)

$$M_z^a = M_0^a \exp(-R_{2\rho}^{a*}t)\cos(\gamma B_1^a t), \qquad [2a]$$

which, for the coupled transverse component, gives

$$M_{y'}^a = M_0^a \exp(-R_{2\rho}^{a*}t)\sin(\gamma B_1^a t). \qquad [2b]$$

For Δz^a where rf inhomogeneity is small, Eqs. [2] reflect the fact that the dominant factor in the time evolution of $\mathbf{M}^a$ is a B_1^a-driven periodic nutational motion.

Similarly, in the Δz^{b} region spins are still underdamped ($\gamma B_1^{\mathrm{b}} > R_{2\rho}^{\mathrm{b}*}$) and oscillate as

$$M_z^{\mathrm{b}} = M_0^{\mathrm{b}} \exp(-R_{2\rho}^{\mathrm{b}*}t)\cos(\gamma B_1^{\mathrm{b}}t) \qquad [3a]$$

$$M_{y'}^{\mathrm{b}} = M_0^{\mathrm{b}} \exp(-R_{2\rho}^{\mathrm{b}*}t)\sin(\gamma B_1^{\mathrm{b}}t). \qquad [3b]$$

However, as compared to the active region, oscillation is expected to be significantly damped due to the increased $\gamma\Delta B_1^{\mathrm{b}}$ term contributing to $R_{2\rho}^{\mathrm{b}*}$. According to Fig. 3 the nutational frequency γB_1^{b} is slower, but not very much so, than in the active region, and therefore we may anticipate that $\gamma B_1^{\mathrm{a}} > \gamma B_1^{\mathrm{b}} \gg R_{2\rho}^{\mathrm{b}*}$.

In the region Δz^{c} where $\gamma B_1^{\mathrm{c}} < R_{2\rho}^{\mathrm{c}*}$, oscillation is overridden by damping, and the decay of the longitudinal magnetization is approximated as

$$M_z^{\mathrm{c}} = M_0^{\mathrm{c}} \exp(-R_{2\rho}^{\mathrm{c}*}t). \qquad [4]$$

In this case the behavior of the transverse component $M_{y'}^{\mathrm{c}}$ has no simple analytical approximation, but is expected to be of biexponential character (13): after a transient increase, it monotonically decays toward steady state.

Returning to the concept of phase randomization, clearly the quick destruction of net magnetization due to a full dephasing of nutating spins in the zy' plane (rather than relaxation) in an inhomogeneous B_1 field is associated with the *underdamped* case, i.e., typically with high-power irradiation. Thus for a given $\gamma B_1(z) \neq$ constant profile, higher B_1 fields ensue quicker phase destruction (8, 11). In the *overdamped* case the full fanning-out of isochromatic magnetization components cannot evolve: the process is in effect stopped in its initial stage by heavy damping. The detected signal is therefore *always* positive irrespective of the applied pulse width pw.

Without making a firm commitment to any specific physical picture underlying the $\Delta z^{\mathrm{a}}/\Delta z^{\mathrm{b}}/\Delta z^{\mathrm{c}}$ model of the total sample volume, three scenarios suggest themselves for consideration. (i) We assume $\gamma B_1(z)$ to have, as a first approximation, a symmetric trapezoidal profile, i.e., $\gamma B_1^{\mathrm{a}}(z) =$ constant along Δz^{a} and $d\gamma B_1^{\mathrm{tr}}(z)/dz =$ constant along Δz^{tr}. Correspondingly, Δz^{b} and Δz^{c} both experience the same degree of rf inhomogeneity, and therefore γB_1^{b} and γB_1^{c} fall into the high-power and low-power classes by virtue of distance from the edge of the coil. (ii) The Δz^{c} region is assumed to become overdamped due to extensive rf inhomogeneity, rather than low power. This model rests on the premise that immediately outside Δz^{a}, the field $\gamma B_1^{\mathrm{tr}}(z)$ falls according to an increasingly steeper slope $d\gamma B_1^{\mathrm{tr}}(z)/dz$. We envision both Δz^{b} and Δz^{c} as occupying only those parts of Δz^{tr} which directly skirt the coil; thus γB_1^{a}, γB_1^{b}, and γB_1^{c} may actually be on the same order of magnitude. Up to a distance Δz^{b} from the coil end, limited rf inhomogeneity keeps the system in the underdamped range, but farther away, in Δz^{c}, inhomogeneity becomes sufficiently large for overdamping to prevail although γB_1^{c} may be on the order of 10^5 rad s^{-1} for typical hard pulses. (iii) It may seem attractive to associate Δz^{b} with the upper and Δz^{c} with the lower (or vice versa) coil ends. However, this would translate into assuming that the $\gamma B_1(z)$ profile is not only highly asymmetric with respect to the upper and lower ends, but this asymmetry is notoriously (i.e., in a wide range of probes) such that at one end an overdamped, while at the other end an underdamped, transition-band spin response is generated. The $\gamma B_1(z)$ plots appearing in the literature (1, 2, 7–9) do not indicate any such asymmetry. Moreover, since the magnetization evolving in a B_1 field is damped by rf inhomogeneity in a time $1/\gamma\Delta B_1$, while during free precession it is damped by B_0 inhomogeneity in a time T_2^*, in the absence of any obvious correlation between B_1 and B_0 inhomogeneities, model (iii) does not explain why the overdamped outer wings are *always* broader than the underdamped inner wings. For these reasons scenario (iii) will be ignored here.

In practice probably both schemes (i) and (ii) contribute to the observed behavior of transition-band signals. However, if the nonoscillatory response of the outer wings were to be *dominantly* due to the weakness, rather than inhomogeneity, of the B_1^{c} field, the time evolution of transition-band spins under the influence of a hard pulse should be highly sensitive to transmitter offset. Actually a difference in the multiple-revolution off-resonance response of transition-band signals and the main resonance only becomes perceivable if the transmitter offset is on the order of 1000 Hz. (By setting the transmitter frequency 200 Hz away from the CHCl$_3$ resonance, the obtained response is almost identical in fine details to the on-resonance behavior shown in Fig. 3.) This supports the substantial contribution of the second model.

FURTHER ASPECTS OF FIGURES 1–3

The resonances due to Δz^{b} and Δz^{c} are typically much broader than the active-volume signal (Fig. 2) as a result of increasingly poor B_0 homogeneity outside the active coil region (7, 15). Susceptibility-related, coil-induced B_0 gradients (7) probably contribute to this problem, but improving shimming techniques (9) are expected to give better results in this regard. For the studied nonspinning concentrated CHCl$_3$ sample, careful but conventional shimming gave an inner- and outer-wing linewidth of $\Delta\nu_{1/2}^{\mathrm{b}} \approx 4$ Hz and $\Delta\nu_{1/2}^{\mathrm{c}} \approx 8$ Hz, respectively (the linewidth of the main resonance for a small-angle observation pulse was typically $\Delta\nu_{1/2}^{\mathrm{a}} \approx 1.7$ Hz which, owing to the presence of radiation damping, decreased substantially upon detuning the probe to give $T_2^* \approx 0.28$ s—see below). These widths are reduced by spinning the sample, but the ensuing modulation effects (7) are undesired during the study of transition-band signals. Since

a T_2^*-related decay can be ignored on the timescale of B_1-pulse-induced evolution of magnetization, differences in the linewidths $\Delta \nu_{1/2} = 1/\pi T_2^{i*}$ serve only to be helpful in monitoring the separate behaviors of Δz^i spins in a strong B_1 field. If Δz^i spins all gave approximately the same linewidths, their different damping characteristics in B_1 would still interfere with null-point detection, as demonstrated below in the case of pulse-width calibrations on spinning samples.

Although for simplicity we make no distinction between the upper and lower transition bands, there is no reason to assume that signals coming from the upper regions $\Delta z^{b'}$ and $\Delta z^{c'}$ behave exactly as those coming from the lower regions $\Delta z^{b''}$ and $\Delta z^{c''}$. In addition to assigning somewhat different rf field strengths to these regions ($\gamma B_1^{b'} \neq \gamma B_1^{b''}$ and $\gamma B_1^{c'} \neq \gamma B_1^{c''}$), the pertinent resonance frequencies $\omega_0^i = \gamma B_0^i$ may also differ slightly ($\omega_0^{c'} \neq \omega_0^{b'} \neq \omega_0^a \neq \omega_0^{b''} \neq \omega_0^{c''}$) due to tiny variations of the main field B_0 along z. This explains the slight asymmetry of the lineshapes in Fig. 2. In this respect the lineshapes of the inner and outer wings, when treated as only two resonances, are not necessarily Lorentzian. Therefore the single T_2^{b*} and T_2^{c*} values derived from the estimated linewidths according to $\Delta \nu_{1/2}^{b,c} = 1/\pi T_2^{b,c*}$ and assigned to the Δz^b and Δz^c regions are only convenient approximations. Sometimes finer splittings or spikes within the inner wing can also be observed, which might arise from differences in the upper- and lower-end effects, specific shimming adjustments, environmental disturbances, a variety of acoustic phenomena (16), or possibly the existence of small segments of relatively high rf homogeneity within the falling $\gamma B_1(z)$ profile of the Δz^{tr} region. Although such details are ignored here, some of them may increase in proportion in multiple nadir and zenith passes, since the inner and outer wings both diminish faster in intensity than the main signal. All these effects, including the possible difference in the nutational frequencies of $\mathbf{M}^{b'}$ and $\mathbf{M}^{b''}$, might contribute to the disintegration of multiple-revolution transition-band lineshapes (Fig. 3).

In Fig. 1b the nonoscillatory behavior of the outer wings corresponds to the net response of *all* isochromatic layers δz^c that compose Δz^c. Since within the Δz^c region the rf power falls sharply, spins resident in δz^c layers that are farther from the edge of the coil will be more resistant to saturation than spins in less distant δz^c layers. As well, the net response of a given succession of "distant" δz^c layers is expected to show more pronounced damping than that of an ensemble of less distant δz^c layers. Thus, when the outer wings are mildly saturated (Fig. 1c), the residual signal gives a more damped aperiodic pw dependence than that observed in Fig. 1b. On increasing γB_2^a further (Fig. 1d), detection is limited to even more distant and saturation-resistant δz^c layers which show even stronger overdamping.

The relatively broad and saturation-resistant outer wings,

which are often detected as a residual "hump" at the base of the main signal upon on-resonance continuous-wave saturation, are commonly attributed to B_0 inhomogeneity (7, 8). Although B_0 inhomogeneity accounts for the *broadness* of the hump, the present results indicate that its *existence* mainly stems from the Δz^c region. The observed aperiodic behavior of this hump (Fig. 1) is incompatible with the notion that it originates mainly from B_0 inhomogeneity: by making the academic assumption that $\gamma B_1(z) = $ constant along the *total* detected sample length and assuming that natural T_1 and T_2 relaxation times are on the order of seconds, for a hard pulse with γB_1 on the order of 10^5 rad s^{-1} the $\gamma B_1^c < R_{2\rho}^{c*}$ condition is only satisfied if T_2^{c*} is on the order of 10^{-6} s (Eq. [1]). This is equivalent to having linewidths on the order of 10^6 Hz (implying an impossibly massive B_0 inhomogeneity problem indeed), instead of the typically observed nonspinning outer-wing linewidths on the order of 10 Hz. Conversely, for a resonance with, say, $\Delta \nu_{1/2} \approx 16$ Hz (i.e., $T_2^{c*} \approx 0.02$ s), the $\gamma B_1^c < R_{2\rho}^{c*}$ condition under perfect B_1 homogeneity would only be valid if $\gamma B_1^c \leq 10$ rad s^{-1}. Such weak rf fields cannot be responsible for the observed behavior of the outer wings, particularly if their above-noted insensitivity to transmitter offset is considered. Consequently when a sufficiently powerful on-resonance continuous-wave saturation is applied, more often than not the observed broad residual signal comes from the Δz^c region rather than being the result of a shimming problem involving the active-volume signal itself.

BLOCH SIMULATIONS

An attempt to simulate the behavior of transition-band signals was based on the Bloch equations (14) extended with the radiation-damping terms (17, 18) to account for the weak radiation damping acting on the active-volume spins of the studied $CHCl_3$ sample (see below)

$$\frac{dM_{x'}^i}{dt} = -(\omega_1 - \omega_0^i)M_{y'}^i - \lambda_2^i M_{x'}^i - \frac{M_{x'}^i M_z^i}{T_{rd}^i M_0^i} \quad [5a]$$

$$\frac{dM_{y'}^i}{dt} = (\omega_1 - \omega_0^i)M_{x'}^i + \gamma B_1^i M_z^i - \lambda_2^i M_{y'}^i - \frac{M_{y'}^i M_z^i}{T_{rd}^i M_0^i} \quad [5b]$$

$$\frac{dM_z^i}{dt} = -\gamma B_1^i M_{y'}^i - \lambda_1^i (M_z^i - M_0^i) + \frac{(M_{x'}^i)^2 + (M_{y'}^i)^2}{T_{rd}^i M_0^i}, \quad [5c]$$

where ω_1 is the rf angular frequency and ω_0^i and T_{rd}^i denote the average Larmor frequencies and characteristic radiation-damping time constants in the respective Δz^i regions ($i = $ a, b, c) and the driving $\mathbf{B_1}$ field is assumed to be along the rotating frame x' axis. In the absence of B_1 inhomogeneity λ_2^i and λ_1^i simply stand for the rate constants $1/T_2^{i*}$ and $1/T_1^i$, respectively, while in the presence of B_1 inhomogeneity they are also
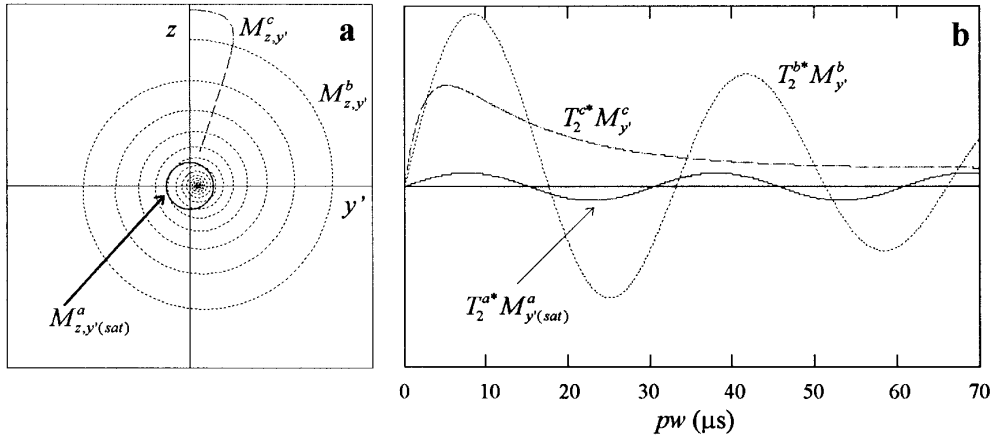
FIG. 4. Simulated time evolution (a) of the $M^i_{z,y'}$ magnetizations (relative intensities are illustrative only) for a theoretical pw = 3000 μs hard pulse and (b) of the $T^{i*}_2 M^i_{y'}$ signal heights of the active-volume ^{13}C satellite (i = a), the inner wings (i = b), and the outer wings (i = c) of the main CHCl$_3$ resonance for a theoretical pw = 70 μs hard pulse as based on Eqs. [5] with the initial condition $M^i_{x',y'(t=0)} = 0$, $M^i_{z(t=0)} = M^i_0$ and the $\mathbf{B_1}$ field being situated along x' in the rotating frame. Parameters were adjusted (20) such that the oscillation of the active-volume ^{13}C satellite magnetization $\mathbf{M}^a_{(sat)}$ (solid circle) is nondamped, and the oscillations of $\mathbf{M}^b$ (dotted line) and $\mathbf{M}^c$ (dashed line) are mildly damped and overdamped, respectively.

assumed, somewhat arbitrarily, to represent the additional damping incurred by the inhomogeneity term $\gamma\Delta B^i_1$ in Eq. [1].

If radiation damping can be ignored and $\omega_1 = \omega^i_0$, for each Δz^i region the system progresses toward the steady-state condition

$$M^i_{x'} = 0 \tag{6a}$$

$$M^i_{y'} = \frac{\gamma B^i_1 \lambda^i_1 M^i_0}{\lambda^i_1 \lambda^i_2 + (\gamma B^i_1)^2} \tag{6b}$$

$$M^i_z = \frac{\lambda^i_1 \lambda^i_2 M^i_0}{\lambda^i_1 \lambda^i_2 + (\gamma B^i_1)^2}. \tag{6c}$$

Note that for a homogeneous rf field Eqs. [6] take the familiar form $M^i_{x'} = 0$; $M^i_{y'} = \gamma B^i_1 T^{i*}_2 M^i_0/[1 + (\gamma B^i_1)^2 T_1 T^{i*}_2]$; $M^i_z = M^i_0/[1 + (\gamma B^i_1)^2 T_1 T^{i*}_2]$. [Inclusion of the radiation damping terms, apart from yielding more complex steady-state solutions (17), has, in the context of the present study, no appreciable effect on the steady-state condition of the system.]

The use of Eqs. [5] to model the behavior of transition-band resonances entails a gross oversimplification: the exact form of the $\gamma B_1(z)$ profile is not known, and it is difficult to incorporate the fact that within Δz^{tr} sensitivity of detection falls, roughly in line with $\gamma B_1(z)$; in the transition band the concept of associating single γB^i_1, λ^i_1, and λ^i_2 values with entire Δz^i regions introduces inevitable errors. Equations [5] were numerically integrated using the Runge–Kutta method (19) and parameterized (20) to approximately match the experimental evolution, relative heights, and linewidths (Figs. 1–3) of all three signal components. As expected, the approach proved to be the most qualified for the least sensitively detected outer wings, in which case a reasonable fit with experiment was

obtained by imposing a $\lambda^c_2 > \lambda^c_1$ relationship on the system (20). (Here λ^c_2 and λ^c_1 depart somewhat from their previous physical meaning of accounting simply for rf inhomogeneity and should be viewed as formally accounting for the sensitivity-of-detection factor as well.) The obtained time evolution of M^b, M^c, and $M^a_{(sat)}$ (the ^{13}C satellite of CHCl$_3$) and that of the respective signal heights $T^{i*}_2 M^i_{y'}$ (21) are shown in Fig. 4. Note that the concept of an effective flip angle θ^c is somewhat vague since θ^c cannot reach 90°. Further fine-tuning of parameters gave good match with the experimental evolution of transition-band signals in the first nadir and zenith passes (Figs. 5 and 6).

All parameters used in the above simulations are interconnected: when searching for a good fit with experiment, a slight change in the value of any parameter open for variation requires the alteration of nearly all other variables. In principle a reasonable fit may be achieved with several parameter sets, and in that sense those used in Figs. 4–6 are representatives of a range of possibilities within the limits of the given relative orders of magnitude (20). However, any change on the order-of-magnitude level renders fitting impossible. For example, the values of γB^c_1, λ^c_2, λ^c_1, M^c_0, and T^{c*}_2 are to be such that they must, after a steep initial rise and within 70 μs, bring the $\mathbf{M}^c$ magnetization close to steady state according to Eqs. [6] so that outer-wing signal heights approach the level of ^{13}C satellites (Fig. 1b). By decreasing γB^c_1 from $\approx 10^5$ rad s^{-1} to, say, $\approx 10^4$ rad s^{-1}, no set of λ^c_2, λ^c_1, or M^c_0 values can be found to match these conditions (although the $\gamma B^c_1 < R^{c*}_{2\rho}$ condition must be satisfied, too much overdamping $\gamma B^c_1 \ll R^{c*}_{2\rho}$ causes a too quick approach to steady state and suppresses the observed transient rising and falling of $M^c_{y'}$—Figs. 1c and 1d). Again, this indicates that γB^a_1, γB^b_1, and γB^c_1 are on the same order of magnitude.

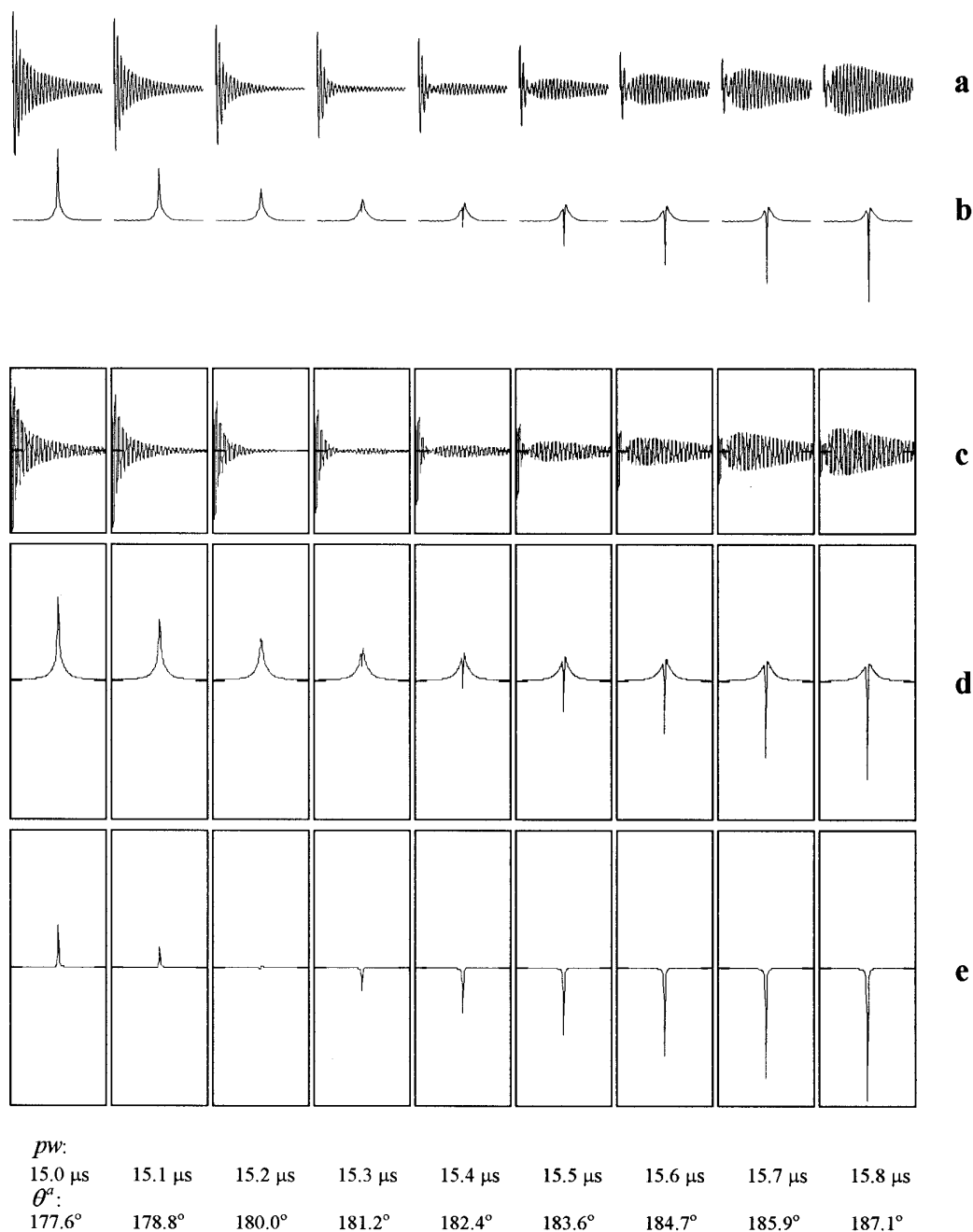| pw:								
15.0 μs	15.1 μs	15.2 μs	15.3 μs	15.4 μs	15.5 μs	15.6 μs	15.7 μs	15.8 μs
θ^a:								
177.6°	178.8°	180.0°	181.2°	182.4°	183.6°	184.7°	185.9°	187.1°

FIG. 5. CHCl$_3$ ^{1}H resonance (nonspinning) passing through the $\theta^a = 180°$ condition. (a) First part of experimental FIDs (0 → 0.5 s) and (b) their Fourier-transformed lineshapes (100 Hz spectral range) obtained with the transmitter offset 50 Hz from the center of the main peak to give a beating pattern to the FIDs (relative to on-resonance irradiation, the offset had no perceivable effect on lineshapes), one transient collected for each pw, relaxation delay 30 s, spectral width 1000 Hz, acquisition time 4 s (the measured 90° pulse width pw$_{90}^{real}$ is 7.6 μs for the active volume). (c) First part of simulated FIDs (0 → 0.5 s) and (d) their Fourier-transformed lineshapes (100 Hz spectral range) composed of $M_{y'}^a + M_{y'}^b + M_{y'}^c$ and calculated from Eqs. [5] such that for the $\mathbf{M}^a$ magnetization pw$_{90}$ = 7.6 μs (20). (e) Behavior of the signal due to $M_{y'}^a$ alone, showing that the "true" 180° pulse width pw$_{180}^{real}$ is at 15.2 μs, while it appears to be at ca. 15.4 μs in (b) and (d).

POSSIBLE IMPLICATIONS

Pulse Width Calibrations

A knowledge of the exact 90° pulse width pw$_{90}$ for the active-volume resonance is a prerequisite for the highest-qual-ity utilization of most pulse sequences and to that end should be determined on the specific sample at hand. This, of course, is routinely done by running a pw-arrayed nadir- or zenith-pass #1 experiment in which pw$_{180}$ or pw$_{360}$ is located on the premise that at such flip angles the intensity of the excited
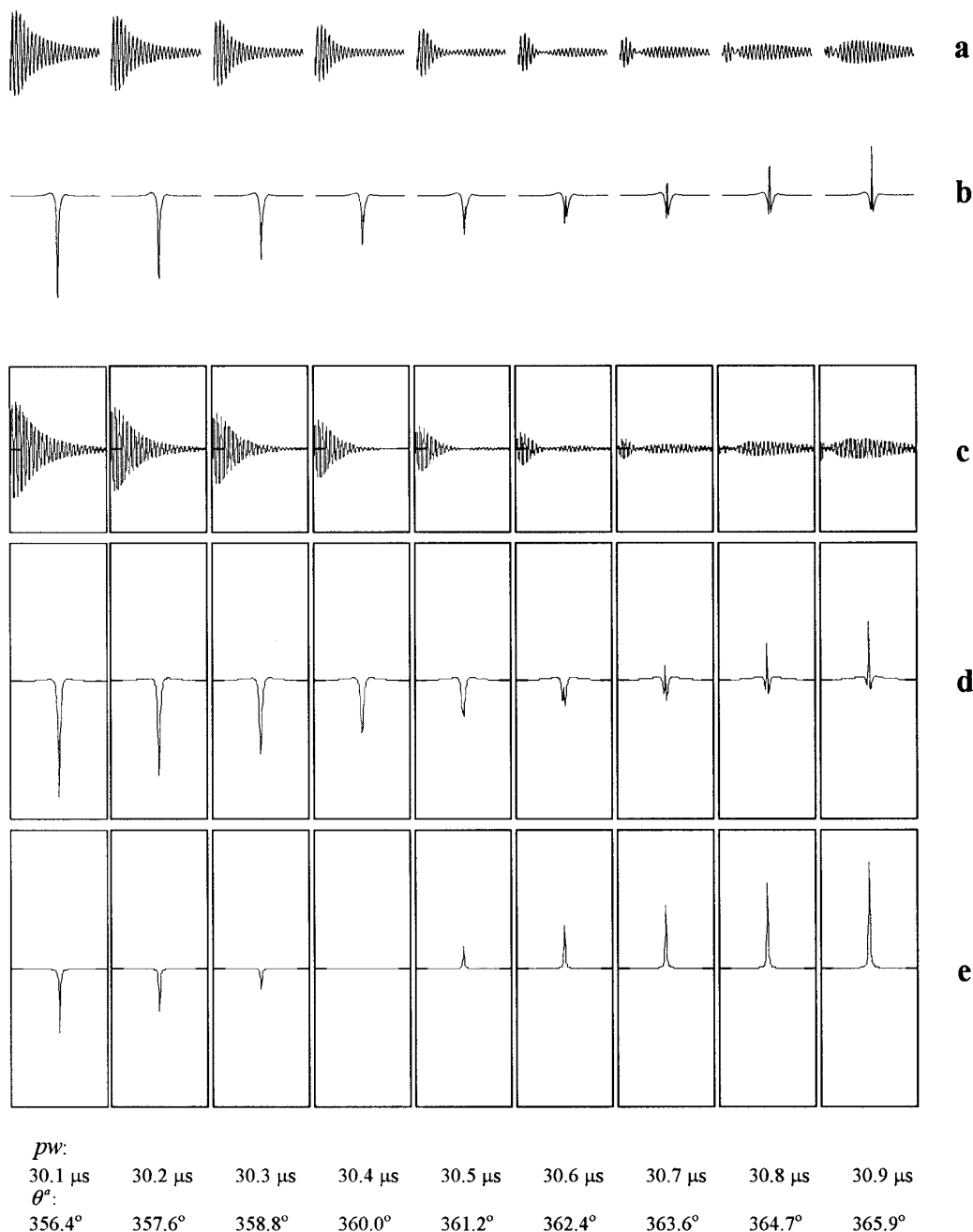
FIG. 6. Behavior of experimental (a, b) and simulated (c, d, e) CHCl$_3$ ^{1}H resonance, as in Fig. 5, but passing through the $\theta^a = 360°$ condition. The "true" 360° pulse width pw$_{360}^{\text{real}}$ is at 30.4 μs, while it appears to be at ca. 30.7 μs in (b) and (d).

signal passes through zero. The procedure is visually straightforward by either interpolating the peak maxima or locating the signal with approximately equally intense positive and negative excursions. However, transition-band signals can falsify the results. For example, according to Figs. 5b and 5d, the apparent 180° pulse width pw$_{180}^{\text{app}}$ would be 15.35 or 15.4 μs (an almost irrelevant difference) depending on whether peak interpolation is used or we look for the "smallest" signal, while the "real" 180° pulse pw$_{180}^{\text{real}}$ is at 15.2 μs (Fig. 5e). Similarly, in

Figs. 6b and 6d, pw$_{360}^{\text{app}} \approx 30.7$ μs, while pw$_{360}^{\text{real}} \approx 30.4$ μs (Fig. 6e). Thus there is a transition-band-related shift (TBRS) in the apparent null point relative to the "true" null point for the active-volume signal. As already alluded to by Hull (5), in suitable cases the latter can be determined by locating the point where the narrow main signal emerges as what we may call a "sprout" from the broader transition-band signal. This "sprouting point" is readily estimated to be at $\approx$15.2 μs in Fig. 5b and 30.4 μs in Fig. 6b, thus giving pw$_{90}^{\text{real}} \approx 7.6$ μs.

The magnitude of the TBRS depends on the relative linewidths $\Delta\nu_{1/2}^a$, $\Delta\nu_{1/2}^b$, and $\Delta\nu_{1/2}^c$: the narrower the main resonance relative to the transition-band signals, the more its behavior is perceived independently from that of the inner and outer wings. Conversely, if $\Delta\nu_{1/2}^a \approx \Delta\nu_{1/2}^b \approx \Delta\nu_{1/2}^c$, the three signal components become intermingled, and the observed pw-dependence in the nadir and zenith areas will approach that of the *combined* $\Delta z^a + \Delta z^b + \Delta z^c$ system, resulting in a larger TBRS and more difficulty in locating the sprouting point. There may be two obvious reasons for such similarity in linewidths: (a) if the main resonance is broadened (due to poor shimming, chemical exchange, etc.), the ensuing broadening of the wider transition-band signals will be relatively less in proportion. An illustration of this effect via artificial line broadening comes from comparing the TBRS of Fig. 7b with that of Fig. 7a, as well as that of Fig. 8b with that of Fig. 8a. A "natural" case is shown in Fig. 9 where pw_{90}^{app} for the exchange-broadened NMe resonance in compound **1** carries a larger TBRS than the narrower OMe signal [note how much more clearly the sprouting point (✳) can be detected for the OMe signal]. (b) With highly sophisticated shimming or by spinning the sample (see below), $\Delta\nu_{1/2}^{b,c}$ may be significantly decreased; intriguingly, this again results in more difficult pw_{90} calibration.

A related but more subtle point is that in the presence of radiation damping, the linewidth becomes a function of pw (*22, 23*) and can be much narrower near the nadir than near the zenith area; this must be taken into consideration during the pw calibration of strong samples (see also below).

With multiple-revolution pulses the broadening factor in the observed TBRS becomes less significant due to a decrease of the transition-band contribution (Figs. 7e and 7f and 8e and 8f).

The resolution enhancement obtained by spinning the sample is relatively larger for the outer wings than for the main signal. Again, this typically increases the TBRS (Fig. 7a → Fig. 7c and Fig. 8a → Fig. 8c) and is the reason for obtaining different pw_{90}^{app} values in spinning vs nonspinning samples.

In some instances the TBRS can lead to a gross miscalibration of pw_{90} (Figs. 7c and 7d), particularly in nadir-pass #1 experiments where the main resonance "works" against the combined $\Delta z^b + \Delta z^c$ signals as opposed to zenith-pass experiments where to some extent the inner and outer wings compensate each other. For zenith-pass experiments the TBRS for the studied $CHCl_3$ sample led to a ≈ 0.1-μs overestimation of pw_{90}; in many experiments even this relatively small error is undesired, e.g., if pw_{90} is used as the basis of calculating selective shaped pulses.

The transition-band contribution near the null point can be easily mistaken for a phase error coming from off-resonance effects (*5*). Such apparent phase errors are typically most conspicuous in spinning samples with relatively narrow outer wings (also making identification of the null point more ambiguous—Figs. 7c and 8c) or broader active-volume signals where one of the outer-wing lobes can be less visible than the other. A closer inspection in such cases shows that the upper and lower excursions of the signal have different widths, which is incompatible with a simple phase distortion. Consequently the application of some line-broadening factor has different relative effects on the positive and negative sides of the signal, and the ensuing TBRS (Figs. 7 and 8) can be a test of whether the distorted lineshape is due to transition-band effects.

The above points imply that apparent sample-to-sample variations in the calibrated pw_{90}^{app} values are a function not only of probe tuning and bulk susceptibility effects (*24*), but also of the linewidths involved! Another implication is that the error caused by the TBRS can be removed by searching for the sprouting point rather than the apparent null point in pw calibrations.

Resolution Enhancement

Since the inner and outer wings are much more strongly damped in a B_1 field than the active-volume signal, the application of multiple-revolution pulses decreases their relative contribution to the main resonance. This results in an improved lineshape regarding the base of the main resonance and can be utilized as a mild resolution enhancement as an alternative to other frequency-domain or time-domain data-manipulation techniques which usually give a greater loss in signal-to-noise ratio (*4b*). By applying a pulse that is, e.g., the five-revolution equivalent of a 90° pulse ($\theta^a = 17 \times 90°$), the achieved resolution enhancement is typically ≈ 0.1 and ≈ 0.25 Hz on spinning and nonspinning samples, respectively (Fig. 10). The obtained resolution enhancement may be increased further by using large transmitter offsets: due to the $\gamma B_1^a > \gamma B_1^b > \gamma B_1^c$ relationship the signal reduction caused by off-resonance effects is larger on the transition-band signals than on the main resonance.

Saturation

As discussed above, the residual signal detected in on-resonance continuous-wave presaturation experiments (Fig. 1) often comes from the transition-band region, as illustrated further in Fig. 11. Full saturation of the "total" signal can be achieved only by severely compromising selectivity.

For on-resonance (semi-)selective rf fields B_2, the decay rate $R_{2\rho}^{a*}$ of the active-volume magnetization (Eq. [1]) is determined mostly by T_2^{a*} rather than rf inhomogeneity, which has little phase-randomizing effect since γB_2^a is on the order of only 10–100 rad s^{-1}. By using Eqs. [5] to simulate the oscillation of M^a in B_2, the mild experimental damping observed as a function of B_2 irradiation time in γB_2^a calibration experiments for $CHCl_3$ was consistent with $\lambda_2^a = 1/T_2^{a*}$ ($T_2^{a*} \approx 0.2$–0.3 s), and the inclusion of any further damping factor into λ_1^a and λ_2^a resulted in too much calculated damping. Thus, in the case of signal "B" (Fig. 11), by simply using $\lambda_2^a = 1/T_2^{a*}$ and $\lambda_1^a = 1/T_1$ ($T_1^B \approx 7$ s, $T_2^{B*} \approx 0.19$ s), Eqs. [6] indicate that saturation with respect to the active-
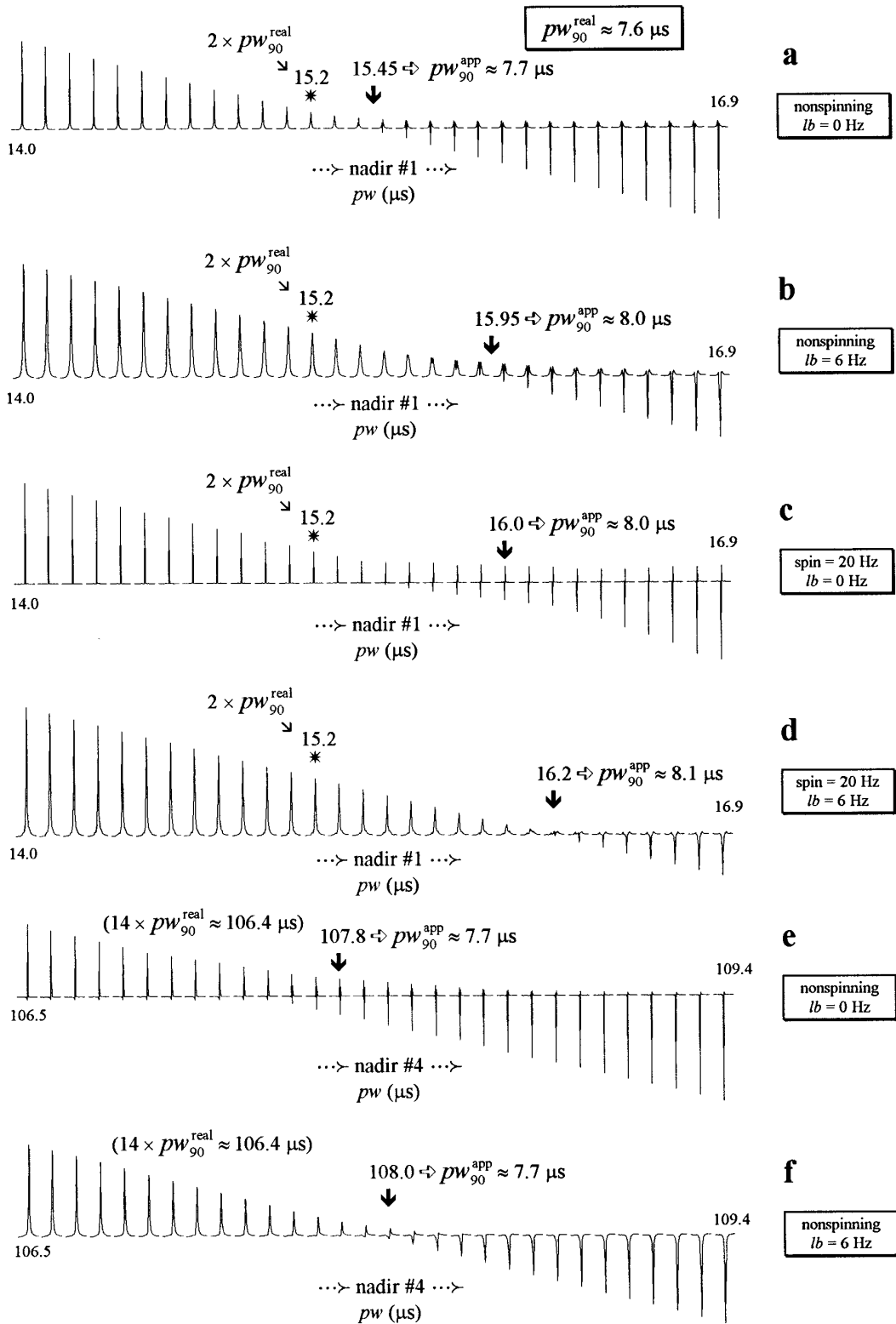
FIG. 7. Pulse-width dependence of the $CHCl_3$ ^1H signal (transmitter on-resonance, $pw_{90}^{real} \approx 7.6$ μs for the active volume), showing the apparent shift of the null point (↓) relative to the sprouting point (✱) [off-scale for (e) and (f), pulse droop assumed to be zero] and the calculated apparent 90° pulse width pw_{90}^{app} depending on the relative widths of the main and transition-band signals as determined from the first (a, b, c, d) and fourth (e, f) nadir passes; pw incremented in 0.1-μs steps, relaxation delay 10 s, acquisition time 4 s, one transient collected for each pw, experiments run in succession (same tuning parameters). "lb" denotes the exponential line-broadening factor applied.
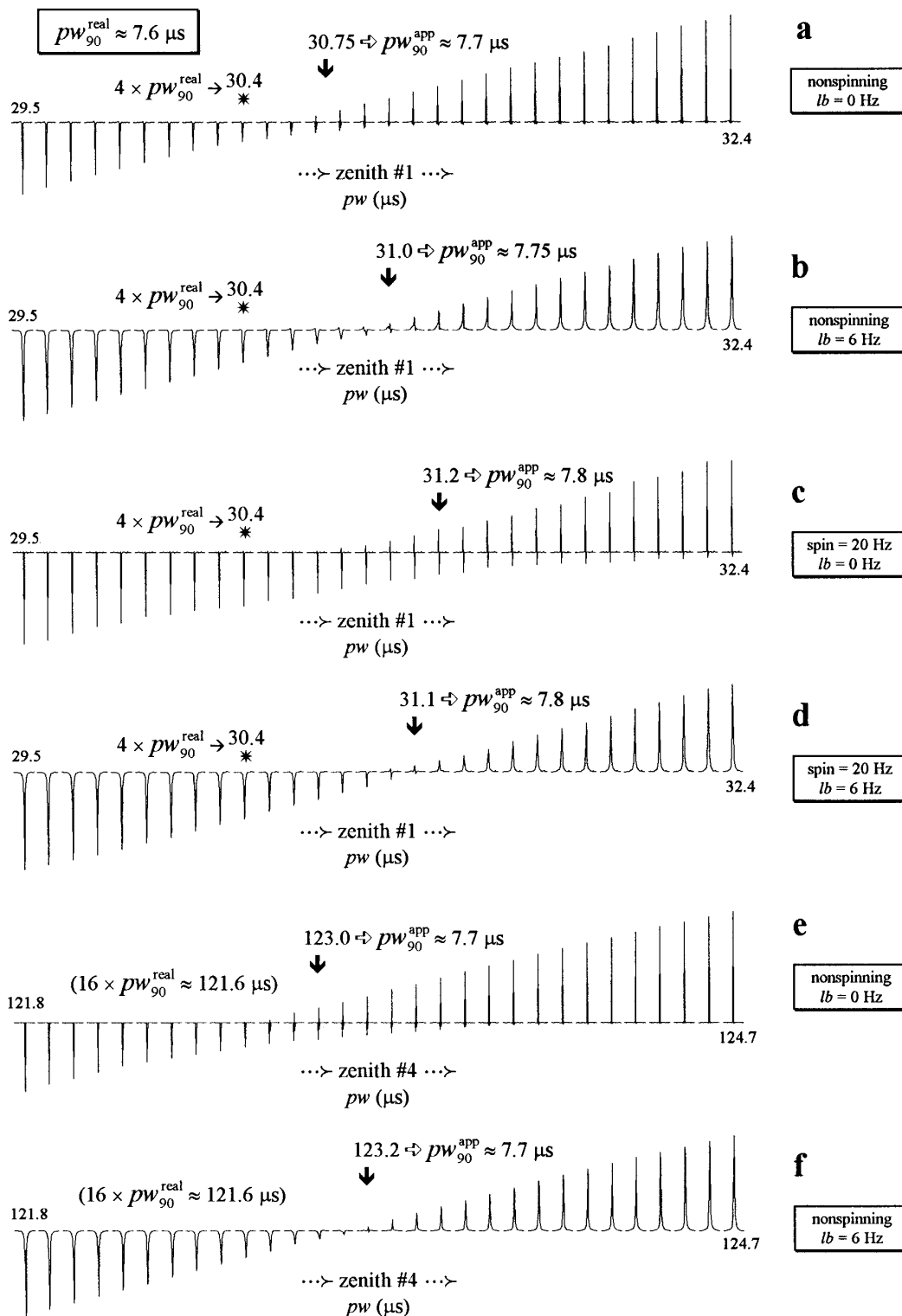
FIG. 8. Pulse-width dependence of the CHCl$_3$ ^{1}H signal, as in Fig. 7, but showing the first (a, b, c, d) and fourth (e, f) zenith passes (relaxation delay 5 s).

volume M_z^a should be practically 100% even for the mildest saturation power $\gamma B_2^a = 71.4$ rad s^{-1} applied in Fig. 11. The residual signal mostly comes from the outer wings which are

saturation-resistant due to the combined effect of experiencing a smaller and more inhomogeneous B_2^c field. The $\gamma B_2(z)$ profile may be significantly different from the $\gamma B_1(z)$ profile,
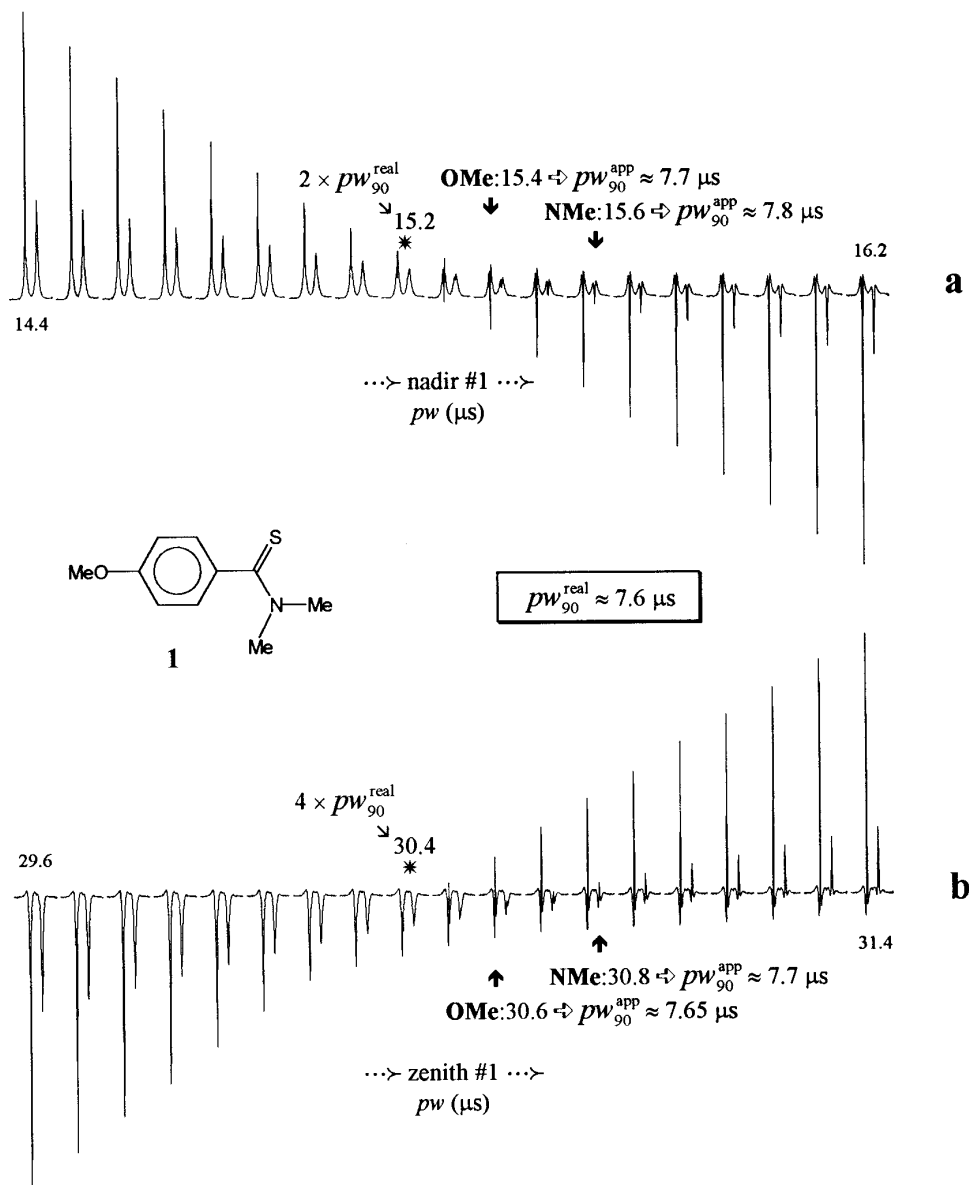
FIG. 9. The first nadir and zenith passes for the OMe ($\Delta\nu_{1/2}^{OMe} = 1.2$ Hz) and the downfield NMe signal ($\Delta\nu_{1/2}^{NMe} = 3.8$ Hz) of compound **1**. The transmitter was set midway between the two signals situated 32 Hz apart; pw incremented in 0.1-μs steps, relaxation delay 10 s (the same result was obtained with 60 s), acquisition time 4 s, one transient collected for each pw, nonspinning sample, lb = 0 Hz, solvent C_6D_6. The apparent null points ($\downarrow$) are shifted differently for the "narrow" and "broad" signal relative to the sprouting point (*).

and an assessment of λ_2^c and λ_1^c is not as readily accessible as for hard pulses. Note, however, that rf inhomogeneity *alone* can reduce substantially the "saturability" of a resonance. For example in the hypothetical case where $\gamma B_2^c = \gamma B_2^a = 71.4$ rad s^{-1}, a relatively mild rf inhomogeneity, represented as $\lambda_2^c = \lambda_1^c = 100$, gives only a 34% saturation of the M_z^c component according to Eqs. [6].

The residual signal stemming from transition-band B_2 inhomogeneity shows some resemblance but is principally unrelated to the well-known "hole-burning" effect caused by the frequency-selective irradiation of a B_0-inhomogeneity-broad-

ened resonance (although some contribution of the latter to the detected "hump" cannot always be ruled out).

Chemical Exchange and Relaxation Measurements

Similarly to pulse-width calibrations, the result of any experiment based on monitoring a resonance passing through the "null" condition may be falsified due to the transition-band contribution. For example in a Forsén–Hoffman-type experiment (*25*), after selective inversion of one of the slowly exchanging NMe resonances in compound **1** (cf. Fig. 9), the
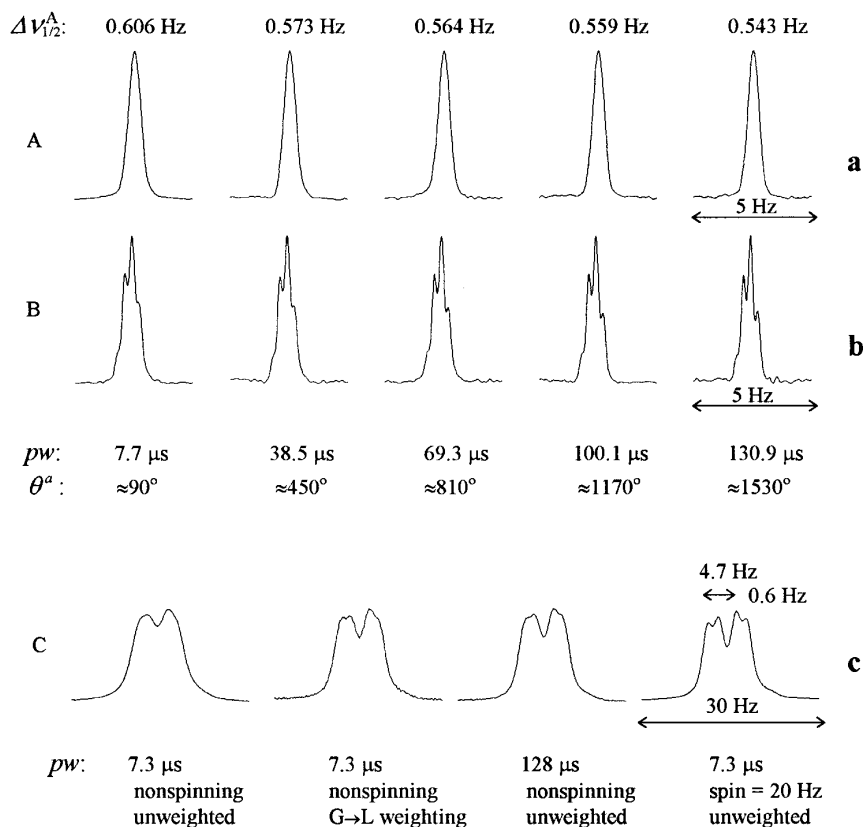
$\Delta\nu_{1/2}^{A}$:   0.606 Hz   0.573 Hz   0.564 Hz   0.559 Hz   0.543 Hz

A

a

5 Hz

B

b

5 Hz

pw: 7.7 µs   38.5 µs   69.3 µs   100.1 µs   130.9 µs
θ^{a}:   ≈90°   ≈450°   ≈810°   ≈1170°   ≈1530°

4.7 Hz
↔ 0.6 Hz

C

c

30 Hz

pw: 7.3 µs   7.3 µs   128 µs   7.3 µs
         nonspinning   nonspinning   nonspinning   spin = 20 Hz
         unweighted   G→L weighting   unweighted   unweighted

FIG. 10.   (a, b) Resolution enhancement by applying multiple-revolution pulses as demonstrated on a ^{1}H resonance showing no scalar couplings (signal "A") and small splittings (signal "B"), obtained from a multiresonance system (sample spinning at 20 Hz, four transients collected for each pw, digital resolution 0.015 Hz/point, no weighting function applied, solvent DMSO-d_{6}). By increasing pw from 7.7 µs (revolution #1) to 130.9 µs (revolution #5), the resolution of signal "A" increased by 0.06 Hz (transmitter offset: 1450 Hz) and the fine splitting of ≈0.3 Hz on signal "B" became more visible (transmitter offset: 1050 Hz). (c) A doublet–doublet signal ("C") obtained under different conditions (one transient): as compared to a Lorentzian-to-Gaussian (G → L) weighting, in a nonspinning sample, a 128-µs pulse gave better exposure of a small coupling (1.6 Hz) which was unresolved in a 7.3-µs experiment (transmitter offset: 438 Hz).

recovery curves driven by magnetization transfer and relaxation *appear* to depend on whether the read pulse is 90° or 270° (Fig. 12). The two cases should, of course, give identical recovery rates, but in practice the transition-band positive outer wings contribute in an opposite sense; thus the zero-crossing point for the inverted upfield resonance appears to be ≈0.15 and ≈0.17 s in the 90° and 270° read-pulse experiments, respectively. The evolution of the downfield NMe signal is similarly affected. As the inverted and noninverted NMe resonances both diminish in intensity during the initial part of recovery, the increasing contribution of the positive outer-wing makes these linewidths progressively different in both experiments.

T_{1} measurements involving inversion-recovery experiments may suffer from similar errors. The possible impact of transition-band effects on the calculated exchange and relaxation rate constants may depend on the relevant timescales involved and has not been fully explored yet. In both cases sample spinning might influence the *apparent* evolution of magnetization similarly to that discussed above in connection with pulse width calibrations. Such differences in inversion-recov-

ery curves obtained in spinning and stationary samples were reported previously (*26, 27*) and were in some cases attributed (*27*) to radiation-damping effects.

Lineshape Tests

The quality of B_{0} homogeneity is traditionally tested by measuring the linewidth at the 50% ($\Delta\nu_{1/2}$), 0.55% ($\Delta\nu_{0.55\%}$), and 0.11% ($\Delta\nu_{0.11\%}$) levels of the maximum peak height of a singlet typically obtained with $\theta^{a} < 90°$. Assuming that shimming is adequately good to provide a properly narrow Lorentzian lineshape for the active-volume resonance, only $\Delta\nu_{1/2}^{a}$ will be a direct measure of shimming quality in the active region. The parameters $\Delta\nu_{0.55\%}$ and $\Delta\nu_{0.11\%}$ will more typically represent B_{0} homogeneity in the transition bands rather than the active coil area.

Radiation Damping

Radiation damping (*28*), i.e., the coupling of the spin system with the receiver coil, has been traditionally associated with very intense resonances typically originating from a solvent
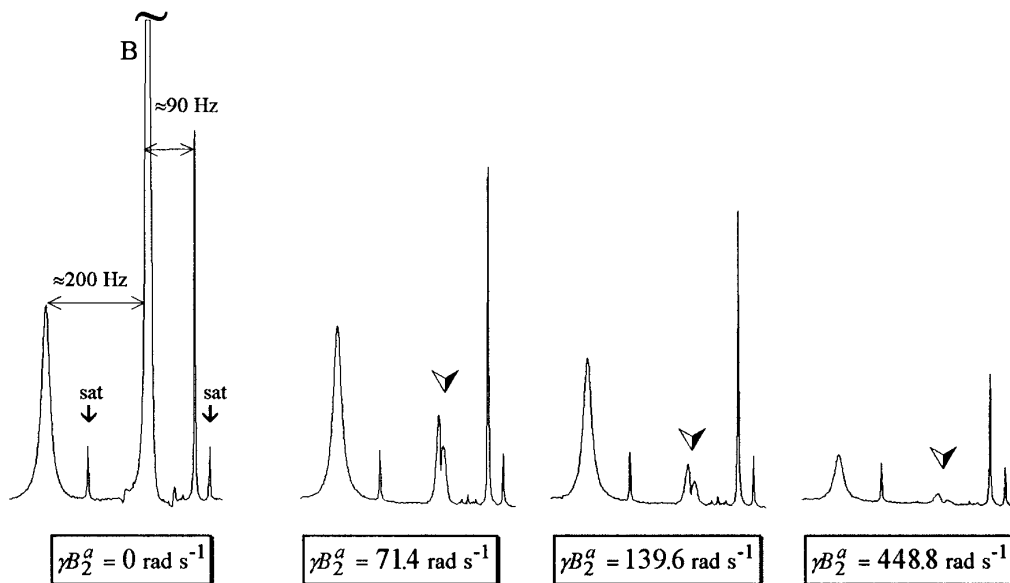
FIG. 11. The effect of saturating signal "B" (cf. Fig. 10); concentrated, nonspinning sample, $T_1^{Ba} \approx 7$ s, $T_2^{Ba*} \approx 0.19$ s, pw = 7.6 μs. A continuous on-resonance presaturating field B_2 was applied (transmitter channel) for 60 s prior to acquisition at various precalibrated γB_2^a power levels (four transients were collected for each γB_2^a value). The outer wings are notoriously resistant to saturation, and nearly full saturation of signal "B" can only be achieved at γB_2^a power levels which also cause significant saturation on the signals 90 and 200 Hz away from the irradiated signal. In the reference spectrum the three resonances shown have a peak-area ratio of 1:8:0.25 (The ^{13}C satellite signals of "B" are only slightly affected by B_2 due to efficient ^{1}H–^{13}C dipolar relaxation.)

signal or highly concentrated samples. With the continuous increase of B_0 fields and the quality factor of probes, the nonlinear effects of radiation damping are increasingly infiltrating the realm of samples of "average" concentrations and have therefore become a renewed focus of research (*29*). Since radiation damping is only operative on the transverse magnetization components, strong radiation damping is associated with $T_{rd} \ll T_2^*$. Strong radiation damping reveals itself in several forms: (1) The linewidth decreases by increasing the pulse flip angle θ from a small value to $\theta = 180° - \epsilon$, where ϵ is an infinitesimal positive angle (*22*). (2) The lineshape is no longer Lorentzian (*22*) and shows substantial side lobes to the central peak at nadir-region flip angles. (3) The peak height H is proportional to the flip angle (*22, 30*), i.e., $H = M_0 T_{rd} \theta$ (up to $\theta = 180° - \epsilon$), as opposed to the sinusoid relationship $H = M_{y'} T_2^* = M_0 T_2^* \sin \theta$ in the absence of radiation damping. (4) The linewidth decreases on detuning the probe. (5) For nadir-region flip angles the initial growth of the transverse magnetization gives a characteristic fish-shaped FID. (6) Inversion-recovery T_1 experiments give typical intensity-jumping effects (*29a*).

While these "markers" are prominent for strong radiation damping, calculations based on Eqs. [5] show that in milder cases when radiation damping is still effective but T_{rd} is only slightly smaller or greater than T_2^*, they have nonconspicuous effects (*31*). In such cases transition-band responses interfere with the assessment of whether radiation damping is present as follows:

(1) In the nadir region the linewidth can differ from the small-pulse-angle linewidth solely due to fact that the relative contribution of the transition-band signals is also a function of θ^a.

(2) In cases where $\theta^a = 180° \pm \delta$ (again δ denotes a small positive angle), the positive inner + outer wings can either conceal or deceptively resemble radiation-damping side lobes.

(3) Mild radiation damping causes an asymmetry in the lobes of the sinusoid $H(\theta)$ profile, as in the case of our CHCl$_3$ test sample (Fig. 1a) for which T_{rd}^a was estimated to be 1.4 s by comparing the small-pulse-angle linewidths obtained on tuned and detuned probes (*28b, 32*). A close inspection of these lobes, particularly if the experiment is run with a finer pw incrementation (*31*), shows that each lobe departs differently from a perfect sinusoid; while radiation damping alone does not account for this behavior, it is consistent with the fact that the transition-band contribution varies along with pw (Figs. 1b, 1c, and 1d). For mild radiation damping, a comparison of the simulated and experimental $H(\theta)$ profiles therefore cannot be reliably used to estimate T_{rd}.

(4) The $\gamma B_1(z)$ profile might change somewhat with probe tuning (*24*), and the consequently altered transition-band response can influence the linewidth independently of the radiation-damping contribution (this possibility was neglected in estimating T_{rd}^a for CHCl$_3$).

(5) In principle the envelope of the FID is, of course, independent of whether $\theta^a = 180° + \delta$ or $\theta^a = 180° - \delta$. In practice, in the range $\theta^a = 180° \pm \delta$ the $\Delta z^{b,c}$ spins provide a quickly decaying positive-phase time-domain signal which ei-
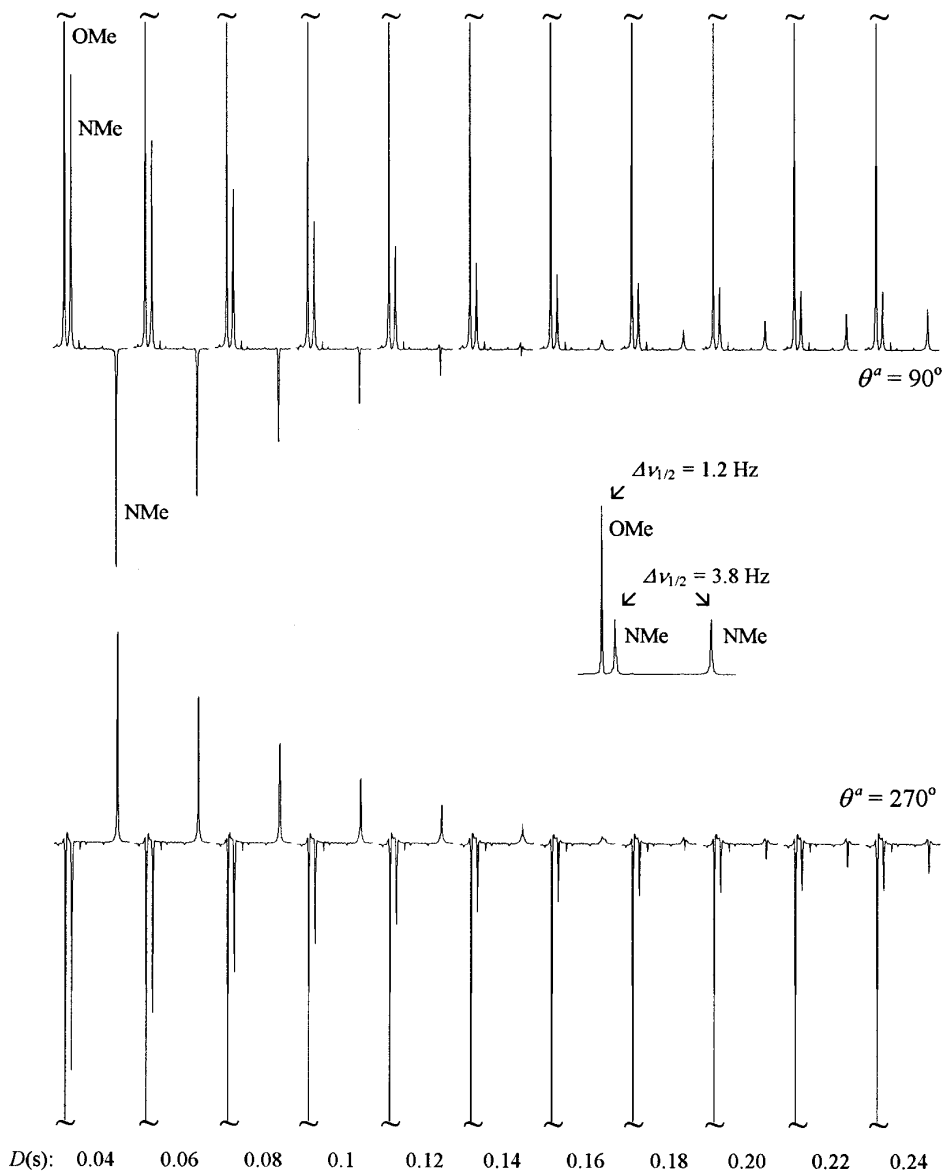
FIG. 12. A Forsén–Hoffman experiment in which the upfield resonance of the exchanging NMe signals in compound **1** has been selectively inverted, then monitored after a delay time D by a 90° or 270° hard read pulse under otherwise identical conditions in the two arrayed experiments (8 transients collected for each D value). The recovery curves as a function of D appear to depend on whether the read pulse is 90° or 270° due to opposite transition-band contributions. In the 270° read-pulse experiment the outer wings of the narrower OMe signal are more prominent than those of the broader downfield NMe signal.

ther reinforces ($\theta^a = 180° - \delta$) or quenches ($\theta^a = 180° + \delta$) the initial part of the FID (Fig. 5). Thus if $\theta^a = 180° - \delta$, $\Delta z^{b,c}$ spins can *conceal* the initial growth of the FID caused by radiation damping of the main resonance; if $\theta^a = 180° + \delta$, they act such that the FID *mimics* a strongly radiation-damped time-domain envelope even if $T_{rd} > T_2^*$, in which case the fish shape should be absent. This effect can occasionally be seen on experimental FIDs reported in the literature (*27*), but as yet has not been commented on or rationalized. Attempts to evaluate T_{rd} from the FID envelope (*27*) should take this factor into account.

(6) Inversion-recovery curves are rather insensitive to weak

radiation damping (*31*) and may be influenced by the TBRS phenomenon as discussed above.

Rf Homogeneity Tests

The standard hard-pulse rf homogeneity test is based on comparing the peak heights H at $\theta^a = 90°$, 450°, and 810° as obtained in a pw-incremented experiment. Unless a microcell is used (*2, 33*), the obtained main-signal peak height ratios will not be directly indicative of B_1^a inhomogeneity only, but will also contain the transition-band contribution potentially inter-mingled with interference coming from radiation damping. By

comparing a $\theta^a = 90°$ with a $\theta^a = 270°$ experiment in which the main-signal decay due to rf inhomogeneity can, as a first approximation, be neglected, we find in repeated measurements in the case of the $CHCl_3$ test sample the peak height ratio to be $H_{270°}/H_{90°} \approx 0.97$, while the ratio of integrated intensities I is $I_{270°}/I_{90°} \approx 0.80$. This difference between integral and peak-height ratios is in itself telling with respect to errors caused by the transition-band contribution. It is sometimes found that $H_{450°}/H_{90°} > H_{810°}/H_{450°}$ under normal conditions, while $H_{450°}/H_{90°} \approx H_{810°}/H_{450°}$ if a microcell is used (2). This can be rationalized in terms of the fact that the outer-wing contribution to the measured main-signal peak height is much larger near $\theta^a = 90°$ than in the vicinity of $\theta^a = 450°$ and $810°$ (cf. Fig. 1). It is noted in this connection that, as an alternative to the nadir- and zenith-pass experiments discussed above, the value of pw_{90} is sometimes obtained by directly measuring the $\theta^a = 90°$ condition as based on the assumption that pw_{90} corresponds to the first positive maximum of the $H(\theta)$ profile. Clearly, even if great care is taken to provide for full relaxation between subsequent pulses and if radiation damping is *known* to be absent, the distortion of the $H(\theta)$ profile due to transition-band signals interferes with the accurate determination of pw_{90} by this method.

CONCLUSIONS

Signals generated in and received from the transition-band area of the rf coil can be treated in terms of two subregions exhibiting a mildly damped oscillatory and an overdamped nonoscillatory time evolution in a B_1 field. Transition-band signals influence in a linewidth-dependent manner the outcome of any experiment in which the active-volume magnetization is monitored as it passes through a condition in which the transverse magnetization generated by the observation pulse is nearly zero, such as in pulse-width calibrations. Further, they interfere with the assessment of whether radiation damping is effective in the studied sample. Other consequences involve rf homogeneity and lineshape tests and a mild resolution enhancement obtained by using multiple-revolution pulses. An awareness of the role of transition-band signals is therefore important on a practical as well as conceptual level. The problem itself, as well as its elimination, deserves further evaluation and research in many areas of high-resolution NMR.

REFERENCES

1. R. E. Hurd, B. K. John, P. Webb, and D. Plant, *J. Magn. Reson.* **99,** 632 (1992).

2. W. Jahnke, *J. Magn. Reson. B* **113,** 262 (1996).

3. (*a*) Gedeon Richter Ltd., Budapest, Hungary; (*b*) EGIS Pharmaceuticals, Budapest, Hungary; (*c*) Technical University of Budapest, Hungary; (*d*) L. Kossuth University, Debrecen, Hungary.

4. R. Freeman, "A Handbook of Nuclear Magnetic Resonance," (a) p. 183, (b) p. 186, Longman, Essex (1987).

5. W. E. Hull, *in* "Two-Dimensional NMR Spectroscopy, Applications for Chemists and Biochemists" (W. R. Croasmun and R. M. K. Carlson, Eds.), p. 95, VCH, New York (1994).

6. S. W. Homans, "A Dictionary of Concepts in NMR," pp. 255–256, Clarendon Press, Oxford (1992).

7. W. Miner and W. W. Conover, *in* "Encyclopedia of Nuclear Magnetic Resonance" (D. M. Grant and R. K. Harris, Eds.), p. 4340, Wiley, New York (1996).

8. I. Hoult, *J. Magn. Reson.* **21,** 337 (1976).

9. Sukumar, M. O'Neil Johnson, R. E. Hurd, and P. C. M. van Zijl, *J. Magn. Reson.* **125,** 159 (1997).

10. D. Neuhaus and M. Williamson, "The Nuclear Overhauser Effect in Structural and Conformational Analysis," p. 19, VCH, New York (1989).

11. C. Torrey, *Phys. Rev.* **76,** 1059 (1949).

12. M. Dobson, E. T. Olejniczak, F. M. Poulsen, and R. G. Ratcliffe, *J. Magn. Reson.* **48,** 97 (1982).

13. K. Madhu and A. Kumar, *J. Magn. Reson. A* **114,** 201 (1995).

14. F. Bloch, *Phys. Rev.* **70,** 460 (1946).

15. N. Chmurny and D. I. Hoult, *Concepts Magn. Reson.* **2,** 131 (1990).

16. P. Gerothanassis, *Prog. NMR Spectrosc.* **19,** 267 (1987).

17. S. Bloom, *J. Appl. Phys.* **28,** 800 (1957).

18. S. Warren, S. L. Hammes, and J. L. Bates, *J. Chem. Phys.* **91,** 5895 (1989).

19. The program MATHCAD Plus 5.0, Mathsoft, Inc., One Kendall Suare, Cambridge, MA 02139, was used for the calculations.

20. Parameters used for the simulated FIDs and spectra shown in Figs. 4–6 are as follows. Figure 4: $\gamma B_1^a = 2.067 \times 10^5$ rad s^{-1} ($pw_{90} = 7.6$ μs for the active volume), $\gamma B_1^b = 1.885 \times 10^5$ rad s^{-1}, $\gamma B_1^c = 1.445 \times 10^5$ rad s^{-1} (Fig. 4a) or $\gamma B_1^c = 1.696 \times 10^5$ rad s^{-1} (Fig. 4b), $M_{0(sat)}^a = 40$ (Fig. 4a) or $M_{0(sat)}^a = 5.5$ (Fig. 4b), $M_0^b = 250$, $M_0^c = 300$ (Fig. 4a) or $M_0^c = 1000$ (Fig. 4b), $\omega_1 = \omega_0^a = \omega_0^b = \omega_0^c = 0$ rad s^{-1}, $\lambda_1^a = \lambda_2^a = 0.001$ s^{-1} (virtually no inhomogeneity damping for the active-volume signal), $\lambda_1^b = \lambda_2^b = 1 \times 10^4$ s^{-1} (Fig. 4a) or $\lambda_1^b = \lambda_2^b = 1.43 \times 10^4$ s^{-1} (Fig. 4b), $\lambda_1^c = 1 \times 10^4$ s^{-1}, $\lambda_2^c = 5 \times 10^5$ s^{-1}, the radiation-damping terms were omitted from Eqs. [5]; for Fig. 4b signal heights $T_2^{j*} M_{y'}$ were calculated with $T_2^{a*} = 0.28$ s, $T_2^{b*} = 0.08$ s, $T_2^{c*} = 0.04$ s. Figures 5 and 6: $\gamma B_1^a = 2.067 \times 10^5$ rad s^{-1} ($pw_{90} = 7.6$ μs for the active volume), $\gamma B_1^b = 1.778 \times 10^5$ rad s^{-1} (for Fig. 5), $\gamma B_1^b = 1.715 \times 10^5$ rad s^{-1} (for Fig. 6), $\gamma B_1^c = 1.445 \times 10^5$ rad s^{-1}, $M_0^a = 100$, $M_0^b = 20$, $M_0^c = 120$, $\omega_1 = 0$ rad s^{-1}, $\omega_0^a = 314.16$ rad s^{-1} ($\omega_0^a/2\pi = 50$ Hz), $\omega_0^b = \omega_0^c = 316.04$ rad s^{-1} ($\omega_0^b/2\pi = \omega_0^c/2\pi = 50.3$ Hz). To calculate the effect of a pulse, Eqs. [5] were used with $\lambda_1^a = 0.1$ s^{-1} and $\lambda_2^a = 3.57$ s^{-1} (this corresponds to $T_1^a = 10$ s and $T_2^{a*} = 0.28$ s with no extra damping included), $\lambda_1^b = \lambda_2^b = 1 \times 10^3$ s^{-1}, $\lambda_1^c = 1 \times 10^4$ s^{-1}, $\lambda_2^c = 5 \times 10^5$ s^{-1} and the radiation-damping terms were omitted. To calculate the FID after the pulse, the following parameters were used in Eqs. [5]: $\lambda_1^a = \lambda_1^b = \lambda_1^c = 0.1$ s^{-1} ($T_1^a = T_1^b = T_1^c = 10$ s), $\lambda_2^a = 3.57$ s^{-1} ($T_2^{a*} = 0.28$ s), $T_{rd}^a = 1.4$ s, $\lambda_2^b = 12.5$ s^{-1} ($T_2^{b*} = 0.08$ s), $\lambda_2^c = 50$ s^{-1} ($T_2^{b*} = 0.02$ s), $T_{rd}^b = T_{rd}^c = 100$ s (virtually no radiation damping). Calculated FIDs were Fourier transformed using 2^{12} data points and a 5×10^{-4} s dwell time (this corresponds to a 1000 Hz spectral width and 2.048 s acquisition time).

21. C. Champeny, "Fourier Transforms and Their Physical Applications," Academic Press, New York (1973).

22. X. Mao and C. Ye, *J. Chem. Phys.* **99,** 7455 (1993).

23. X. Mao, J. Guo, and C. Ye, *Chem. Phys. Lett.* **218,** 249 (1994).

24. R. L. Vold, R. R. Vold, and H. E. Simon, *J. Magn. Reson.* **11,** 283 (1973).

25. S. Forsén and R. Hoffman, *J. Chem. Phys.* **39,** 2892 (1963).

26. B. Blicharska, *J. Mol. Liq.* **52,** 109 (1992).

27. D. Wu and C. S. Johnson, Jr., *J. Magn. Reson. A* **110,** 113 (1994).

28. (*a*) N. Bloembergen and R. V. Pound, *Phys. Rev.* **95,** 8 (1954). (*b*) Abragam, "The Principles of Nuclear Magnetism," p. 73, Clarendon Press, Oxford (1961).

29. (*a*) J. Chen, X. Mao, and C. Ye, *J. Magn. Reson.* **124,** 490 (1997); (*b*) E. L. Hahn, *Concepts Magn. Reson.* **9,** 65 (1997); (*c*) A. Sodickson, W. E. Maas, and D. G. Cory, *J. Magn. Reson. B* **110,** 298 (1996); (*d*) S. Zhang and D. Gorenstein, *J. Magn. Reson. A* **118,** 291 (1996); (*e*) W. E. Maas, F. H. Laukien, and D. G. Cory, *J. Magn. Reson. A* **113,** 274 (1995); (*f*) H. Barjat, G. P. Chadwick, G. Morris, and A. Swanson, *J. Magn. Reson. A* **117,** 109 (1995); (*g*) L. Picard, M. von Kienlin, and M. Décorps, *J. Magn. Reson. A* **117,** 262 (1995); (*h*) P. Broekaert and J. Jeneer, *J. Magn. Reson. A* **113,** 60 (1995); (*h*) D. Abergel, C. Carlotti, A. Louis-Joseph, and J.-Y. Lallemand, *J. Magn. Reson. B.* **109,** 218 (1995); (*i*) C. Anklin, M. rindlisbacher, G. Otting, and F. H. Laukien, *J. Magn. Reson. B* **106,** 199 (1995).

30. X. Mao, D. Wu, and C. Ye, *Chem. Phys. Lett.* **204,** 123–127 (1993).

31. Cs. Szántay, Jr., and Á. Demeter, submitted for publication.

32. M. Gueron and J. L. Leroy, *J. Magn. Reson.* **85,** 209 (1989).

33. I. M. Armitage, H. Huber, D. H. Live, H. Pearson, and J. D. Roberts, *J. Magn. Reson.* **15,** 142 (1974).